EDGE ARTICLE

Near infrared light regulated crystallization-driven self-assembly: a versatile platform for controlled preparation of uniform π-conjugated functional nanostructures

Rang Chen,[a] Sen Zhang,[a] Xiaoyu Huang, [ID] *[a] Guolin Lu,[a] Mitchell A. Winnik[cd] and Chun Feng [ID] *[ab]

Photo-controlled block copolymer self-assembly to modulate the morphology and dimensions of polymer nanoparticles (PNPs) has attracted growing interest. However, most photo-induced polymer self-assembly approaches are dependent on ultraviolet- or visible-light-based photochemical reactions that lead to structural variations of the PNPs. The limited morphology control of these approaches hinders their broad applications. Here we report a novel near-infrared (NIR) light regulated self-seeding strategy for the controlled preparation of uniform π-conjugated nanofibers of a $4\text{-BBT-OPE}_3\text{-P2VP}_{22}$ block copolymer. This approach combines a NIR light induced photothermal effect with living crystallization-driven self-assembly (CDSA). By taking advantage of excellent photothermal activity and crystallinity of the 4-BBT-OPE_3 segment, uniform helical fiber-like micelles could be generated with tunable lengths from ~40 nm to 1.1 μm, photothermal activity and NIR-II emission. The lengths of these fiber-like micelles could be regulated by the time and power of NIR irradiation (808 nm laser). Moreover, the NIR light regulated self-seeding strategy could also be extended to core-crystalline block copolymers that lack a NIR-absorbing group if a NIR-absorbing dye like indocyanine green was added to the solution. Given the appealing merits and versatility of NIR light regulated self-seeding, this work paves a new way toward precise preparation of "smart" functional nanomaterials.

Introduction

Self-assembly is a fundamental and ubiquitous phenomenon in nature.[1] Life itself relies heavily on the dynamic and precise self-assembly of biomolecules such as amino acids, sugars, and phospholipids.[1–3] Among synthetic systems, the self-assembly of block copolymers—an important and rapidly advancing area in nanoscience and nanotechnology—has emerged as a powerful and robust platform for constructing polymeric nanoparticles (PNPs) with variable sizes, morphologies, and compositions, for applications ranging from biomedicine to microelectronics.[4–7] Beyond composition, the size and morphology of PNPs are key

determinants of their properties and functions.[8–11] Consequently, extensive efforts have focused on developing diverse stimulus-responsive self-assembly systems to create size- and morphology-controllable PNPs for "intelligent" materials and devices with adaptable functionalities.[12–14] To date, a variety of stimuli—including pH, temperature, light, ions, enzymes, and reactive radical species—have been employed to regulate self-assembly processes and vary PNP characteristics.[4,15–18] Among these, light stands out for its remote, non-invasive nature and high spatial and temporal precision, making light-responsive polymer self-assembly a particularly promising strategy for generating "intelligent" PNPs with real-time, remote controllability.

Most light-responsive polymer self-assembly systems are based on the structural transformation of a photo-switchable unit through a photochemical reaction (Scheme 1a).[16–18] Specifically, groups such as azobenzenes, spiropyrans, and diarylethylenes are introduced into the polymer building blocks, and these undergo *trans*/*cis* isomerization, ring opening/ring closing or photoaddition reactions to give corresponding products with different chemical structures upon ultraviolet (UV) or visible light irradiation.[16–19] The change in the chemical structure alters the solvophobic/solvophilic balance of the

[a]State Key Laboratory of Fluorine and Nitrogen Chemistry and Advanced Materials, Shanghai Institute of Organic Chemistry, University of Chinese Academy of Sciences, 345 Lingling Road, Shanghai 200032, People's Republic of China. E-mail: cfeng@ecust.edu.cn; xyhuang@mail.sioc.ac.cn; Tel: +86-21-54925310

[b]Shanghai Key Laboratory of Advanced Polymeric Materials, School of Materials Science and Engineering, East China University of Science and Technology, 130 Meilong Road, Shanghai 200237, People's Republic of China

[c]Department of Chemistry, University of Toronto, 80 St. George St, Toronto, Ontario M5S 3H6, Canada

[d]Department of Chemical Engineering and Applied Chemistry, University of Toronto, Toronto, ON M5S 3E2, Canada
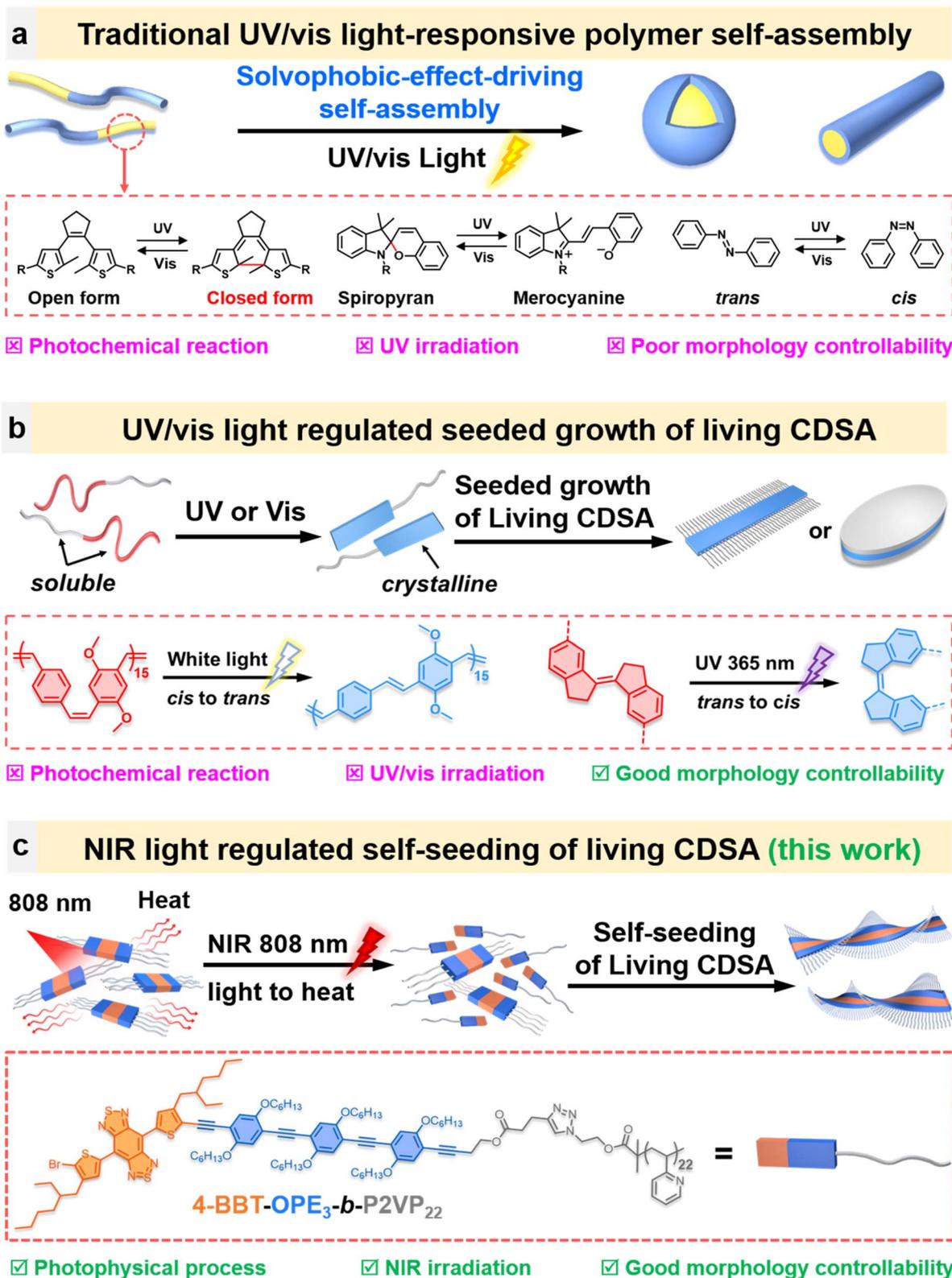
Scheme 1 Strategies of photo-controlled polymer self-assembly to generate PNPs with a tunable size and morphology. (a) Traditional UV/vis light-responsive polymer self-assembly through photoisomerization, ring closing/ring opening, and addition reactions of azobenzenes, spiropyrans and diarylethylenes upon UV and visible light irradiation. (b) Seeded growth of living CDSA *via* UV and visible light induced isomerization. (c) NIR light regulated self-seeding *via* the NIR light induced photothermal effect.

polymer building blocks, leading to changes in the size and morphology of PNPs.

Despite the wide use of this strategy to create a variety of light stimulus-responsive PNPs for diverse applications in catalysis and as biosensors,[16–19] some features of this strategy might impede their broad applications. First, irradiation with UV light is usually required for triggering light-stimulus-responsive polymer self-assembly. Due to the relatively high energy of UV light, irradiation can result in polymer degradation, cross-linking, photo-bleaching or other unexpected side reactions. It can also lead to degradation of the surrounding organic, polymer, or biological matrices.[20,21] For biological applications, another limiting aspect is that UV light has a weak penetration depth owing to the competing absorption of light by biological tissue.[22] A second aspect limiting applications is that photo-induced polymer self-assembly is generally driven by solvophobic effects. These changes lead to PNPs with relatively poor structural or morphological controllability.[16–19,23,24] A third consideration is that the stimulus-responsiveness usually relies on a structural transformation of photo-switchable units of the polymer building blocks.[16–19,23,24] This structural transformation can affect or change the targeted properties of PNPs.[16–19] In this context, the development of novel light controlled polymer self-assembly strategies to resolve these issues is highly desired but remains a great challenge.[25–27]

Living crystallization-driven self-assembly (CDSA) provides an efficient platform to generate uniform one-, two- and three-dimensional nanostructures in a controlled way.[26–48] Two examples of photo-controlled CDSA by seeded growth have been reported recently (Scheme 1b).[26,27] Choi and co-workers reported a photo-controlled growth of a block copolymer containing a core-forming crystalline poly(p-phenylenevinylene) (PPV) segment.[26] A block copolymer with PPV segments in the cis-conformation in solution was mixed with a suspension of pre-formed seed micelles with their trans PPV segments forming the rigid core. Upon irradiation with white light, the PPV segments in the cis-conformation were transformed into the trans-conformation, leading to the epitaxial crystallization of the newly formed trans PPV segments onto the ends of pre-existing PPV-based seeds. The photo-controlled seeded growth strategy enabled the authors to generate uniform nanofibers of controlled length.

In the second example, Mai and co-workers[27] examined an alternating copolymer that they referred to as poly(hexylthienyl trans-stiff-stilbene-alt-ethylene glycol) (P(trans-HTSS-alt-PEG)). In THF, this polymer is soluble, but upon irradiation at 365 nm, the trans stilbene units rearrange to the cis form, which then crystallizes to form lenticular platelet micelles. When a solution of P(trans-HTSS-alt-PEG) was irradiated in THF in the presence of seed micelle fragments obtained by sonication of the platelet micelles, the newly formed cis polymer crystallized epitaxially off the edges of the seed micelles to form larger platelet micelles that were relatively uniform in size. In this way, they carried out a photo-driven seeded growth CDSA experiment in which the size of resulting platelets could be regulated by UV irradiation.

Self-seeding is another approach for living CDSA. It relies on a feature unique to semi-crystalline polymers, that different regions of the crystal have different degrees of crystallinity, leading to a distribution of melting points or dissolution temperatures. This property can be used as a versatile platform to generate uniform one-, two- and three-dimensional nanostructures in a controlled way.[31,32,48] In a self-seeding experiment, a suspension of polymer crystallites is heated to a temperature where some but not all of the polymer dissolves. Upon cooling, the surviving crystallites serve as seeds for the epitaxial growth of the polymer that dissolved. The size of the resulting nanostructures is dependent on the degree of dissolution of seeds, which in turn is modulated by the annealing temperature.

While self-seeding experiments are normally carried out by direct heating of a sample with an oil bath or a heating mantle, one can also heat a sample by the near infrared (NIR) light-induced photothermal effect.[49–51] Thus, we hypothesized that the dimensions of semicrystalline nanostructures might be manipulated by NIR light irradiation, combining the photothermal concept with a self-seeding strategy (Scheme 1c). On the basis of our previous work on the generation of uniform nanofiber-like micelles containing a donor–acceptor π-conjugated core with photothermal activity by CDSA,[52,53] we inferred that the temperature of micellar solution might be modulated by the NIR photothermal effect. In this way, the morphology and the dimensions of the micelles obtained might be regulated by NIR light irradiation. This strategy has some intriguing merits. First, NIR light with lower energy and longer wavelength than UV light will exhibit limited structural destruction. It also has a higher capacity for penetrating biological tissue. Second, the photothermal effect is a typical photophysical process, and thus changes in the chemical structure of building blocks upon irradiation can be avoided for regulating the dimensions of the nanostructures.

To test the hypothesis, we synthesized a block copolymer containing a 4-BBT-OPE$_3$ core forming block that combines the excellent crystallinity of OPE segments with the NIR photothermal activity of BBT units and a P2VP (P2VP = poly(2-vinylpyridine)) corona-forming segment (Scheme 1c). Here BBT = benzobisthiadiazole, OPE = oligo(p-phenylene ethynylene), and the subscript represents the number of repeat units. Using this sample as a model, its NIR light regulated self-seeding behavior was examined. Helical fiber-like micelles of 4-BBT-OPE$_3$-b-P2VP$_{22}$ were formed in ethanol, and these micelles, under 808 nm laser irradiation, exhibited both photothermal activity and NIR II emission. By taking advantage of the intrinsic photothermal activity of 4-BBT-OPE$_3$ segments, uniform fiber-like micelles with controlled lengths ranging from ~40 nm to 1.1 μm were formed by NIR light induced self-seeding with negligible variation of the structure of the micelles. The number-average length (L_n) of micelles could be regulated by the time and power of NIR irradiation. Of course, these micelles are not suitable for biomedical applications. However, to test their behavior in a simulated environment, we exposed them to NIR light through samples of chicken tissue with thicknesses up to 4 mm. Under these conditions, we were still able to observe NIR light induced self-seeding to regulate the length of fiber-like micelles. By adding a group similar to

BBT as an extra photothermal moiety, NIR light induced self-seeding can be extended to other coil-crystalline block copolymers without photothermal activity.

Results and discussion

Micelle structure

Our experimental design combines the excellent crystallinity of OPE segments with the NIR photothermal activity of BBT. Alkyne-terminated 4-BBT-OPE$_3$ was synthesized by an iterative Sonogashira coupling reaction (Schemes 1c and S1–S3). Subsequently, alkyne-terminated 4-BBT-OPE$_3$ was connected with azide-terminated P2VP by a Cu-catalyzed alkyne–azide cycloaddition reaction to give 4-BBT-OPE$_3$-b-P2VP$_{22}$ (Scheme 1c and Fig. S1–S17, details about its synthesis and characterization are provided in the SI). Matrix-assisted laser desorption/

ionization time-of-flight mass spectrometry, ^{1}H nuclear magnetic resonance and gel permeation chromatography analyses confirmed the structure of 4-BBT-OPE$_3$-b-P2VP$_{22}$ (additional discussion on the synthesis and characterization of 4-BBT-OPE$_3$-b-P2VP$_{22}$ in the SI, Fig. S7–S17).

To examine the CDSA behavior of 4-BBT-OPE$_3$-b-P2VP$_{22}$, a suspension of 4-BBT-OPE$_3$-b-P2VP$_{22}$ in ethanol (0.05 mg mL^{-1}), a typical selective solvent for the P2VP segment, was heated at 80 °C for 30 min and then cooled/aged at 25 °C for 24 h (heating/cooling protocol, Fig. 1a).

As shown in Fig. 1b and c, fiber-like micelles with a uniform width of ~18 nm were obtained. Upon closer inspection, one can see a helical (wave-like) structure, for the micelles rather than the commonly observed linear structure (Fig. 1b and S18–S20). After the micelles were stained with phosphotungstic acid, which has a high affinity towards basic P2VP chains,[54] the
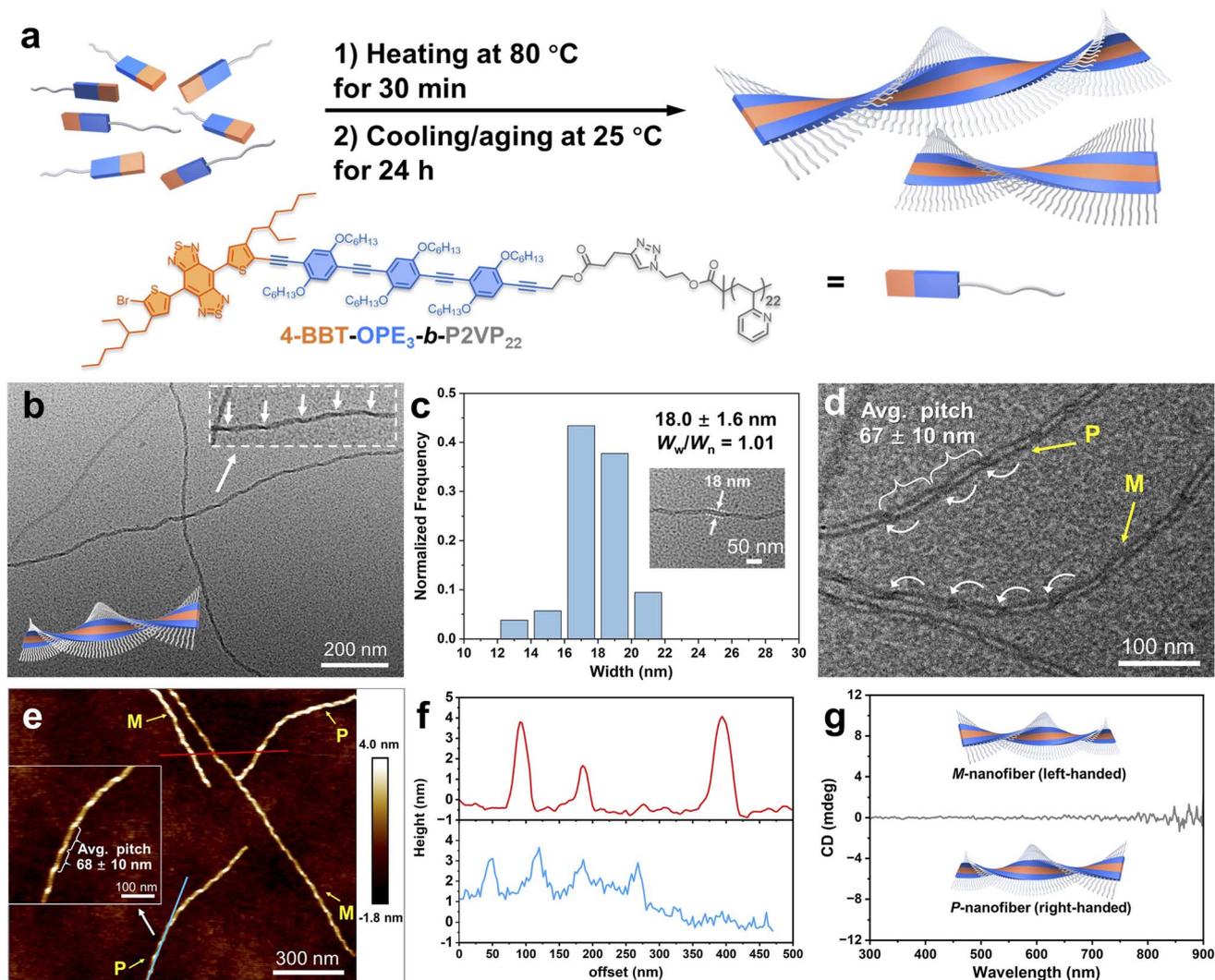

Fig. 1 4-BBT-OPE$_3$-containing helical fiber-like micelles obtained by the heating–cooling protocol. (a) Schematic illustration of formation of helical fiber-like micelles of 4-BBT-OPE$_3$-b-P2VP$_{22}$. (b and d) TEM images and (c) histogram of the width distribution of helical fiber-like micelles of 4-BBT-OPE$_3$-b-P2VP$_{22}$ formed in ethanol (0.05 mg mL^{-1}) by the heating/cooling protocol. (e) AFM image of helical fiber-like micelles of 4-BBT-OPE$_3$-b-P2VP$_{22}$ and (f) height profiles along the red and blue lines shown in (e). (g) CD spectrum of a micellar solution of 4-BBT-OPE$_3$-b-P2VP$_{22}$ (0.1 mg mL^{-1} in ethanol).

helical structure became much more distinguishable with a regular pitch (P) of ~67 nm (Fig. 1d and S18–S20). Atomic force microscopy (AFM) analysis also revealed the formation of helical fiber-like micelles with a height of ~2–4 nm and a regular pitch of ~68 nm (Fig. 1e, f and S21), close to the value obtained by TEM (Fig. 1d). Of note, we found that the helical fiber-like micelles consisted of a racemic (left- and right-handed) mixture of isomers, as indicated in Fig. 1d and e. A circular dichroism (CD) measurement showed a negligible Cotton effect (Fig. 1g), further demonstrating formation of equal amounts of racemic isomers of helical fiber-like micelles.

There are, in principle, two different ways that 4-BBT-OPE$_3$ units can be incorporated into helical fiber-like micelles, and we refer to them as the two-column or single-column packing modes (Fig. 2a).[55] To get more information about the packing modes of 4-BBT-OPE$_3$ units, we carried out simulations on two- and single-column tetrameric packing modes of 4-BBT-OPE$_3$ with Materials Studio 7.0, using the Condensed-phase Optimized Molecular Potentials for Atomistic Simulation Studies (COMPASS) force field (Fig. 2b, c and S22–S27).[56,57] The results revealed that the lowest energy configuration of the two-column packing mode with slipping (θ_S) and rotation angles (θ_R) of 31.8° and 0.3°, respectively, was about 12 kcal mol^{-1} lower than that of the single-column packing mode, along with about 112 Å^2 larger overlapping area of packing units (Fig. 2b, c and S22–S26). The simulation results indicated that two-column packing was likely more favorable. This notion was supported by the

observation that the width of the micelle core was about 4.2 nm (Fig. 2d and S27), which is consistent with the value (~4.3 nm) estimated on the basis of proposed two-column packing mode (Fig. 2e). A typical peak at $q = 17.7$ nm^{-1} (d-spacing = 0.35 nm) attributable to π–π stacking of 4-BBT-OPE$_3$ units (Fig. 2f and S28) appeared in the grazing incidence wide angle X-ray scattering (GIWAXS) pattern of the film of micelles of 4-BBT-OPE$_3$-b-P2VP$_{22}$, showing that the distance between adjacent 4-BBT-OPE$_3$ units is about 0.35 nm. Given the regular pitch of fiber-like micelles (~67 nm), the rotation angle (θ_R) between adjacent 4-BBT-OPE$_3$ units was estimated to be ~0.9° ($\theta_R = 180°/(P/d\text{-spacing}) = 180°/(67/0.35)$), higher than the value obtained by the simulation (0.3°). For the simulation of the packing of the core-forming 4-BBT-OPE$_3$ segments, the corona-forming P2VP was not taken into account in order to reduce the computational cost. Previous reports showed that the steric repulsion within corona chains would also affect the packing of core-forming units.[58,59] We presume that the 4-BBT-OPE$_3$ units of 4-BBT-OPE$_3$-b-P2VP$_{22}$ adopt a much larger rotation angle than the simulated value to reduce steric repulsion between adjacent P2VP chains.

Spectroscopic properties

Subsequently, the photophysical properties of 4-BBT-OPE$_3$-b-P2VP$_{22}$ were examined, both in THF (0.05 mg mL^{-1}), a good solvent for both 4-BBT-OPE$_3$ and P2VP segments, and in ethanol, a selective solvent for the P2VP block. In THF, a peak at
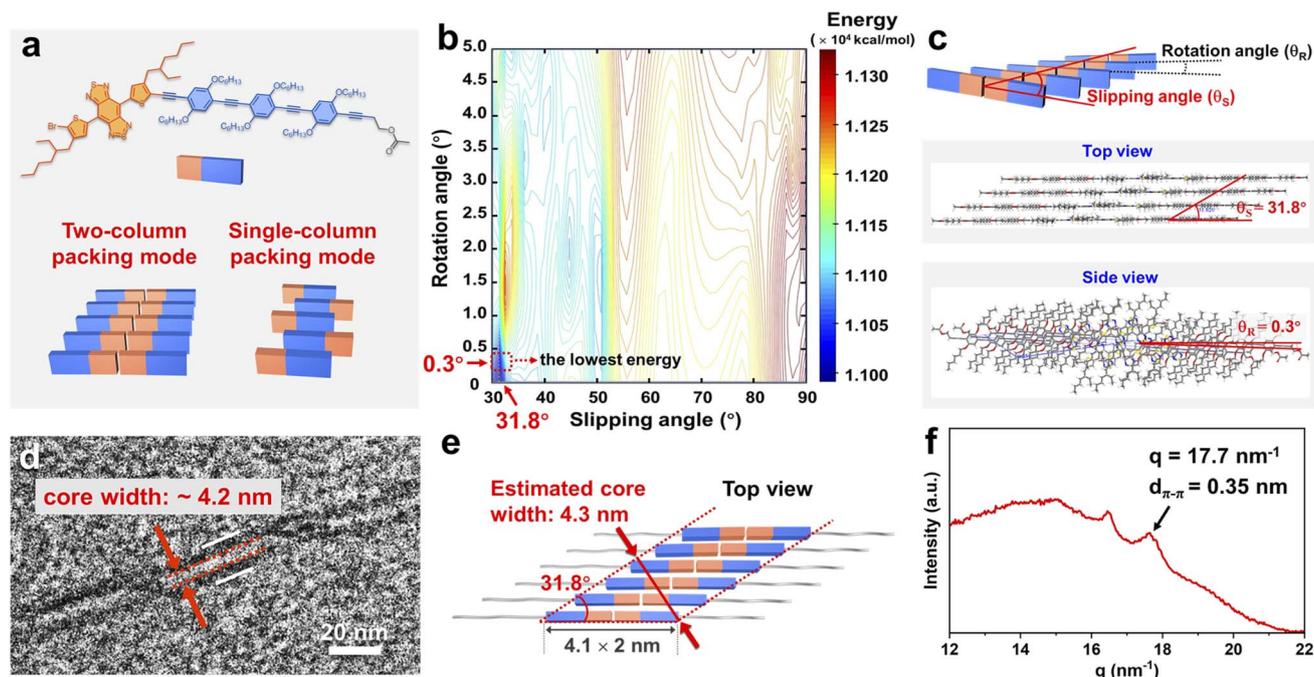

Fig. 2 Packing modes of helical fiber-like micelles. (a) Schematic illustration of possible two- and single-column packing modes for 4-BBT-OPE$_3$ to form helical fiber-like micelles. (b) Energy dependence of aggregates of 4-BBT-OPE$_3$ with two-column packing mode with slipping (θ_S) and rotation (θ_R) angles obtained by simulation with Materials Studio 7.0 using the COMPASS force field. (c) Two-column octameric packing mode of 4-BBT-OPE$_3$ with the lowest energy configuration as obtained by the simulation. (d) TEM image of micelles of 4-BBT-OPE$_3$-b-P2VP$_{22}$ stained with phosphotungstic acid. (e) Estimated core width on the basis of the two-column packing mode with θ_S of 31.8°. (f) GIWAXS pattern of the film of micelles of 4-BBT-OPE$_3$-b-P2VP$_{22}$.
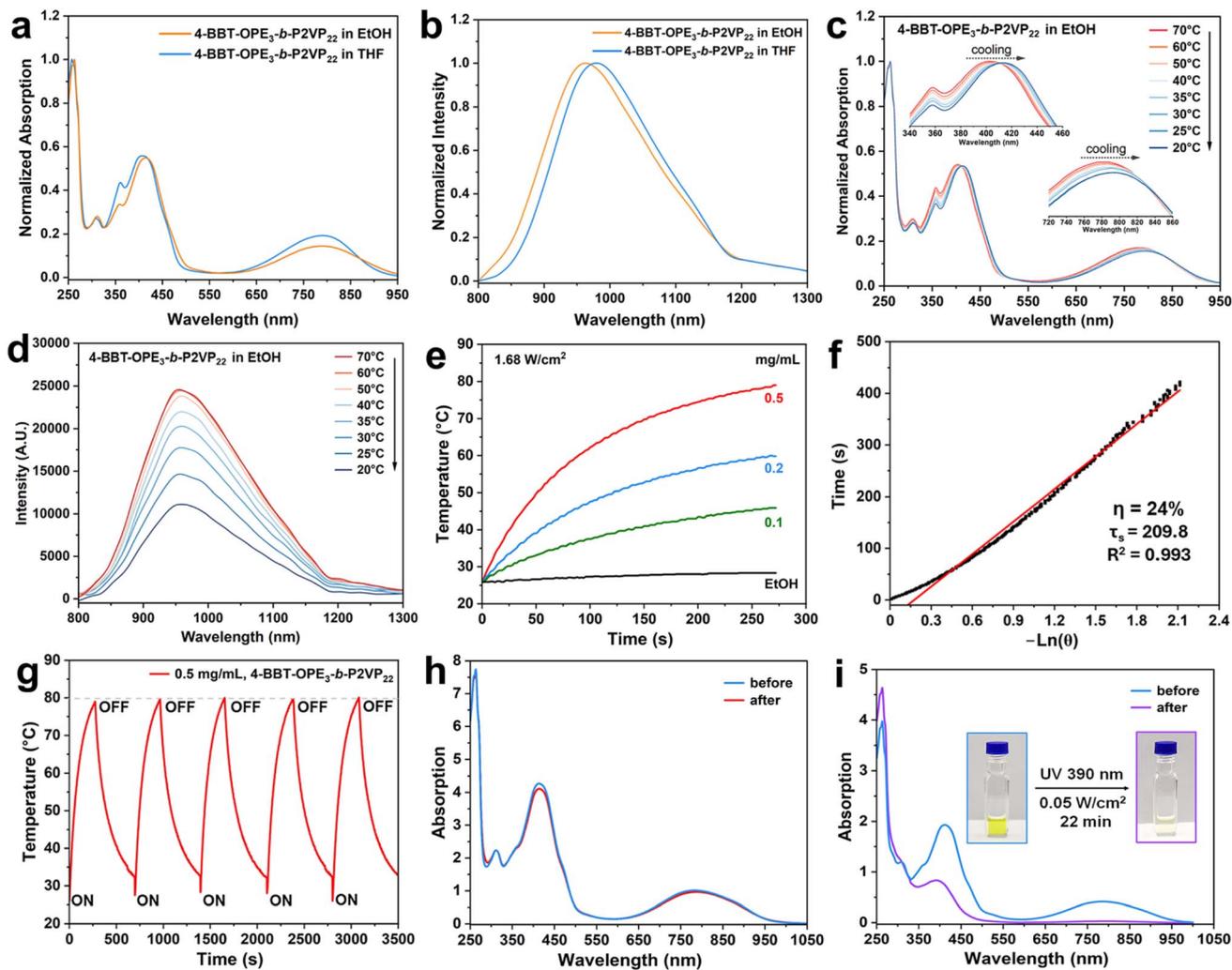
Fig. 3 NIR emission and photothermal activity of 4-BBT-OPE3-containing fiber-like micelles. (a) UV-vis-NIR absorption and (b) fluorescence spectra of 4-BBT-OPE$_3$-b-P2VP$_{22}$ in ethanol and THF (0.05 mg mL^{-1}). Temperature-dependent (c) UV-vis-NIR absorption and (d) fluorescence spectra of 4-BBT-OPE$_3$-b-P2VP$_{22}$ in ethanol (0.05 mg mL^{-1}). (e) Photothermal curves of ethanol and a micellar solution of 4-BBT-OPE$_3$-b-P2VP$_{22}$ in ethanol with different concentrations (1.68 W cm^{-2}). (f) Photothermal conversion efficiency of 4-BBT-OPE$_3$-b-P2VP$_{22}$ (0.5 mg mL^{-1} and 1.68 W cm^{-2}). (g) Photothermal curves of micellar solution (0.5 mg mL^{-1}) of 4-BBT-OPE$_3$-b-P2VP$_{22}$ in ethanol with five on/off cycles of irradiation (1.68 W cm^{-2}). UV-vis-NIR absorption spectra of micellar solutions of 4-BBT-OPE$_3$-b-P2VP$_{22}$ before and after (h) NIR (808 nm, 1.68 W cm^{-2}, and 0.5 mg mL^{-1}) and (i) UV (390 nm, 0.05 W cm^{-2}, and 0.2 mg mL^{-1}) irradiation for 22 min.

406 nm and a shoulder at 790 nm attributed to the absorbance of OPE$_3$ and BBT segments, respectively, appeared in the UV-vis-NIR absorption spectrum (Fig. 3a). The absorbance of the corresponding ethanol solution exhibited about a 7 nm red-shift from 407 nm to 414 nm and 1 nm red-shift from 790 nm to 791 nm compared to the peaks of the THF solution (Fig. 3a). With an excitation wavelength of 780 nm, the emission band of the ethanol solution showed an 18 nm blue-shift from 978 nm to 960 nm in comparison with that of the THF solution (Fig. 3b). Of note, for the spectrum in ethanol, the emission band tailed to >1300 nm with a maximum at 960 nm and an absolute photoluminescence quantum yield of 0.5% (Fig. 3b and S29). This observation implies that the nanofibers may be appealing candidates for NIR-II fluorescence imaging as tested in Fig. S30. In addition, the temperature-dependent UV-vis-NIR absorption and emission spectra in ethanol were also recorded (Fig. 3c and

d). With decreasing temperature from 70 °C to 20 °C, the absorption maxima red-shifted from 402 nm to 413 nm, accompanied by a 16 nm red-shift for the shoulder from 779 nm to 795 nm (Fig. 3c). The NIR emission with a maximum at 960 nm showed obvious quenching with a decrease of ∼55% as the temperature decreased from 70 °C to 20 °C (Fig. 3d). These phenomena indicated that 4-BBT-OPE$_3$ units likely adopted a J-aggregate mode to form the micelle core (Fig. 3a and c),[60,61] consistent with the simulated results (Fig. 2e).

Photothermal activity

The micelle solutions in ethanol exhibited photothermal activity under irradiation with an 808 nm laser (1.68 W cm^{-2}). As the micellar solution (0.5 mg mL^{-1} in ethanol, 0.22 mL) was exposed to the laser for 270 s, the solution temperature

increased from 26 °C to 79 °C with a photothermal conversion efficiency of 24% (Fig. 3e, f and S31). In contrast, ethanol in the absence of micelles exhibited a negligible temperature change (<2.5 °C, Fig. 3e). The temperature elevations remained at nearly the same level over five cycles of laser irradiation (Fig. 3g). Moreover, the absorption bands and ^1H NMR spectra of the corresponding copolymer also exhibited negligible variation after five cycles of laser irradiation (Fig. 3h and S32). These phenomena indicated the high chemical stability of 4-BBT-

OPE$_3$-b-P2VP$_{22}$ against NIR irradiation (Fig. S33). Under UV irradiation, evidence for photochemical decomposition was observed. As the micellar solution of 4-BBT-OPE$_3$-b-P2VP$_{22}$ was exposed to UV light (390 nm and 0.05 W cm^{-2}) for 22 min, the absorbance at 412 nm decreased along with the disappearance of the shoulder at 790 nm, indicative of UV-light-induced photobleaching (Fig. 3i).

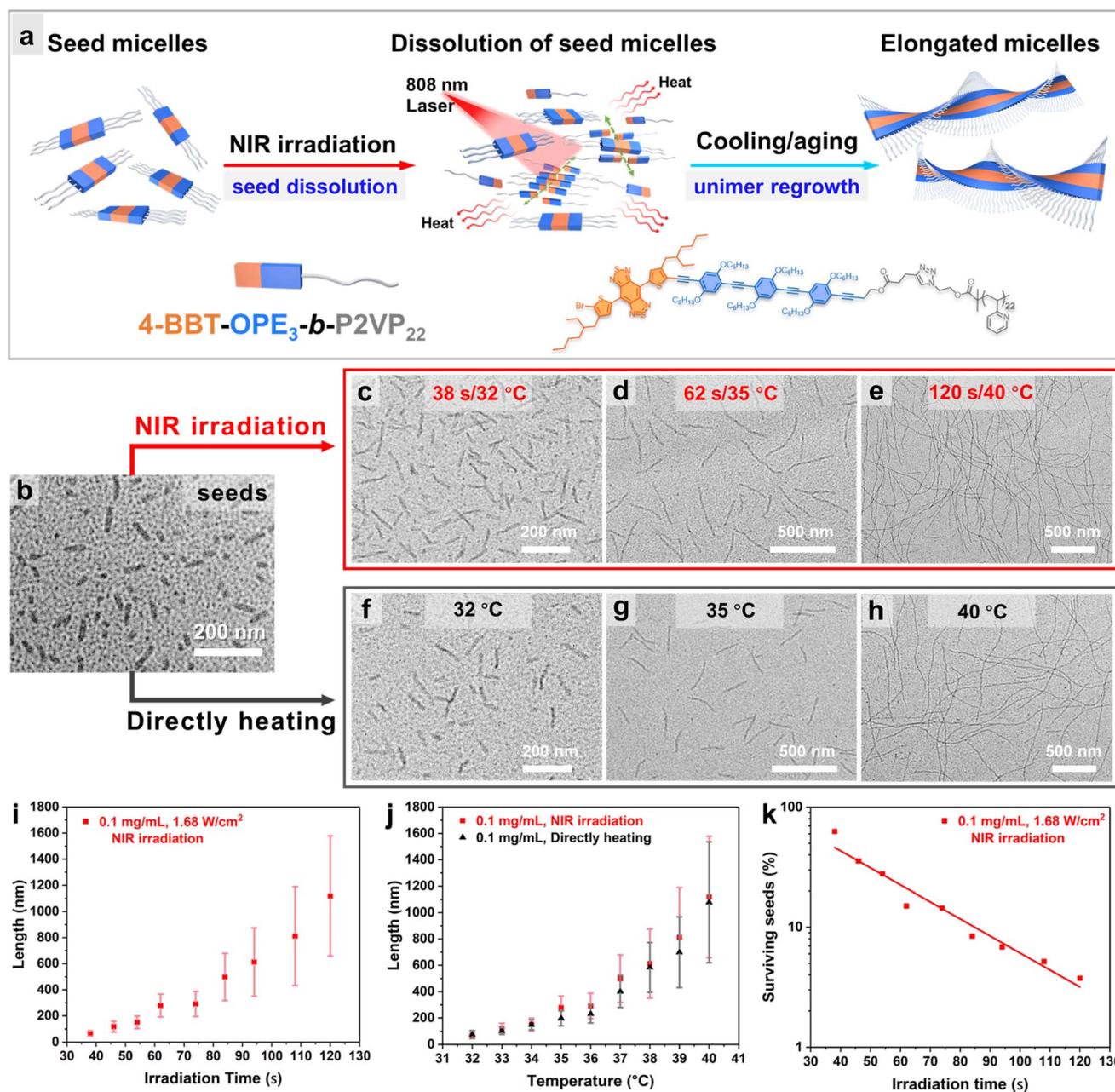We also found that both the heating rate and ceiling temperature of the micellar solutions increased with the

Fig. 4 NIR regulated self-seeding of 4-BBT-OPE3-containing block copolymers. (a) Schematic illustration of NIR light regulated self-seeding. TEM images of (b) seed micelles of 4-BBT-OPE$_3$-b-P2VP$_{22}$; micelles obtained by NIR light irradiation (0.1 mg mL^{-1}) for (c) 38 s, (d) 62 s and (e) 120 s; and micelles obtained by self-seeding under direct heating at (f) 32 °C, (g) 35 °C and (h) 40 °C. (i) Dependence of L_n of micelles of 4-BBT-OPE$_3$-b-P2VP$_{22}$ on NIR irradiation time. (j) Dependence of L_n of the resulting micelles on the heating temperature obtained by NIR irradiation and direct heating regulated self-seeding of 4-BBT-OPE$_3$-b-P2VP$_{22}$. (k) Dependence of fractions of surviving seed micelles on the heating temperature (irradiation time) in NIR irradiation regulated self-seeding of 4-BBT-OPE$_3$-b-P2VP$_{22}$.

concentration of micelles and the irradiation power of the 808 nm laser (Fig. 3e and S34). These observations indicate that the solution temperature can be manipulated by the laser power, irradiation time and polymer content. For example, when the micelle concentration was decreased to 0.2 and to 0.1 mg mL^{-1}, the maximum temperature of the solution reached 60 °C and 46 °C, respectively, after 270 s of laser irradiation (Fig. 3e).

We then attempted to induce self-seeding to regulate the length of fiber-like micelles of 4-BBT-OPE$_3$-b-P2VP$_{22}$ via NIR irradiation (Fig. 4a). To this end, a dispersion of 4-BBT-OPE$_3$-b-P2VP$_{22}$ (0.5 mg mL^{-1}) in ethanol was heated at 80 °C for 40 min, followed by cooling/aging at −20 °C to give seed micelles[62] (Fig. 4b and S35, L_n = 42 nm, L_w/L_n = 1.11). Subsequently, aliquots of seed micelles (diluted to 0.1 mg mL^{-1} in ethanol) were subjected to NIR laser irradiation (808 nm and 1.68 W cm^{-2}) for 38, 46, 54, 62, 74, 84, 94, 108 and 120 s, causing the solution temperature to increase from 26 °C to 32 °C, 33 °C, 34 °C, 35 °C, 36 °C, 37 °C, 38 °C, 39 °C and 40 °C, respectively (Fig. 4a and S36). The solutions were then allowed to cool/age at 25 °C for 48 h. TEM analysis revealed that uniform fiber-like micelles of different lengths were obtained, with L_w/L_n below 1.22 (Fig. 4c–e, i, j, S36 and Table S2). The L_n of micelles was 67, 118, 151, 279, 291, 498, 613, 811 and 1119 nm for the irradiation time of 38, 46, 54, 62, 74, 84, 94, 108 and 120 s, respectively (Fig. 4i, S36 and Table S2), demonstrating an intriguing feature of modulating the length of uniform fiber-like micelles by the irradiation time. Note that these length distributions are not particularly narrow. For a Gaussian distribution of lengths, L_w/L_n is related to the standard deviation σ of the length distribution by the expression:[63]

$$\frac{L_w}{L_n} - 1 = \left(\frac{\sigma}{L_n}\right)^2 \tag{1}$$

In Fig. 4i, it appears that the width of the micelle length distribution increased with irradiation time, and in Fig. 4j we see that a similar phenomenon occurred for self-seeding under direct heating. The σ values of micelles formed increased with the annealing temperature of the solution, but the effect is more subtle. This can be seen if we consider the coefficient of variation of the length distribution (CV(%) = σ/L_n × 100). The original seed micelles are characterized by (L_n = 42 nm, L_w/L_n = 1.11, σ = 14 nm, CV = 34%, Table S2). Conditions that increased the micelle length to 100 to 200 nm led to a decrease in the length distribution (L_w/L_n < 1.10, CV < 30%, $e.g.$ Table S5), as expected for a self-seeding process. [31] Longer micelles were characterized by a modest increase in the length distribution. For example, irradiation for 120 s heated the solution to 40 °C and formed micelles with (L_n = 1119 nm, L_w/L_n = 1.17, σ = 460 nm, CV = 41%, Table S2) upon cooling. This type of length broadening in a self-seeding experiment has been observed previously and was attributed to shear-induced micelle fragmentation associated with convection in the solution.[64] These thin micelles are known to be fragile.[65] Two features of the experiment affect fragmentation. The first is that longer

micelles are more susceptible to fragmentation.[66] The second factor is the temperature at which micelle growth takes place upon cooling the solution after annealing. If micelle growth is delayed until the solution has cooled, the convection forces are weak, and the micelle length distribution is narrow. If micelle growth occurs at higher temperatures, the convection forces can promote fragmentation.

We can use the mean lengths of the micelles obtained by self-seeding to calculate the percentage of the initial seed micelles $P_{s,T}$ that survived the heating protocol at different irradiation times (temperatures).

$$P_{s,T} = (L_{n,S}/L_{n,T}) \times 100 \tag{2}$$

Here, $L_{n,S}$ is the mean length of the initial seeds and $L_{n,T}$ is the mean length of the micelles obtained after cooling to room temperature. As seen in Fig. 4k (Table S2), $P_{s,T}$ decreased exponentially with the temperature (irradiation time). This is a key characteristic of the self-seeding process.[31]

For comparison, the self-seeding of 4-BBT-OPE$_3$-b-P2VP$_{22}$ micelles in ethanol was carried out using a direct heating protocol. Aliquots of seed micelles (Fig. 4b, L_n = 42 nm, L_w/L_n = 1.11, 0.1 mg mL^{-1}, the same seeds used for the NIR light induced self-seeding) were subjected to heating in an oil bath at temperatures ranging from 32 °C to 40 °C for 30 min, followed by cooling/aging at 25 °C for 48 h. TEM analysis revealed that uniform fiber-like micelles with L_w/L_n below 1.18 and L_n values of 76, 102, 148, 197, 231, 401, 584, 699 and 1078 nm were formed for annealing temperatures of 32 °C, 33 °C, 34 °C, 35 °C, 36 °C, 37 °C, 38 °C, 39 °C and 40 °C (Fig. 4f–h, j, S37 and Table S5). The variation of L_n of the micelles with heating temperature for NIR laser irradiation and direct heating exhibited a similar trend (Fig. 4j). All these observations show that self-seeding of 4-BBT-OPE$_3$-b-P2VP$_{22}$ induced by NIR irradiation followed a typical seed-dissolution and unimer-regrowth mechanism.[48] Specifically, upon NIR light irradiation, the photothermal activity of 4-BBT-OPE$_3$ units resulted in an increase of solution temperature, and this led to the partial dissolution of seed micelles (Fig. 4a and S38). Longer laser irradiation led to a higher percentage of dissolved seeds, resembling the characteristics of a normal heat-regulated self-seeding process, indicating that the self-seeding behavior was not significantly sensitive to the way of heating. One interesting difference between the two heating protocols is that, for direct heating, the micellar solutions have to be in physical contact with the heating source, whereas with NIR light irradiation, uniform fiber-like micelles of controlled lengths can be prepared in a remote and "noninvasive" manner.

Since micelle concentration and laser power combine to influence the photothermal effect, we investigated the influence of micelle concentration on the self-seeding of 4-BBT-OPE$_3$-b-P2VP$_{22}$ seed micelles (Fig. 5a and e). To this end, aliquots of seed micelles (Fig. 4b, L_n = 42 nm, L_w/L_n = 1.11) with concentrations of 0.05 and 0.2 mg mL^{-1} were exposed to NIR light irradiation (808 nm and 1.68 W cm^{-2}) for different times. The solution temperatures reached values of 32 °C to 40 °C (37 °C for the 0.05 mg mL^{-1} sample, Fig. S39 and S40), followed by
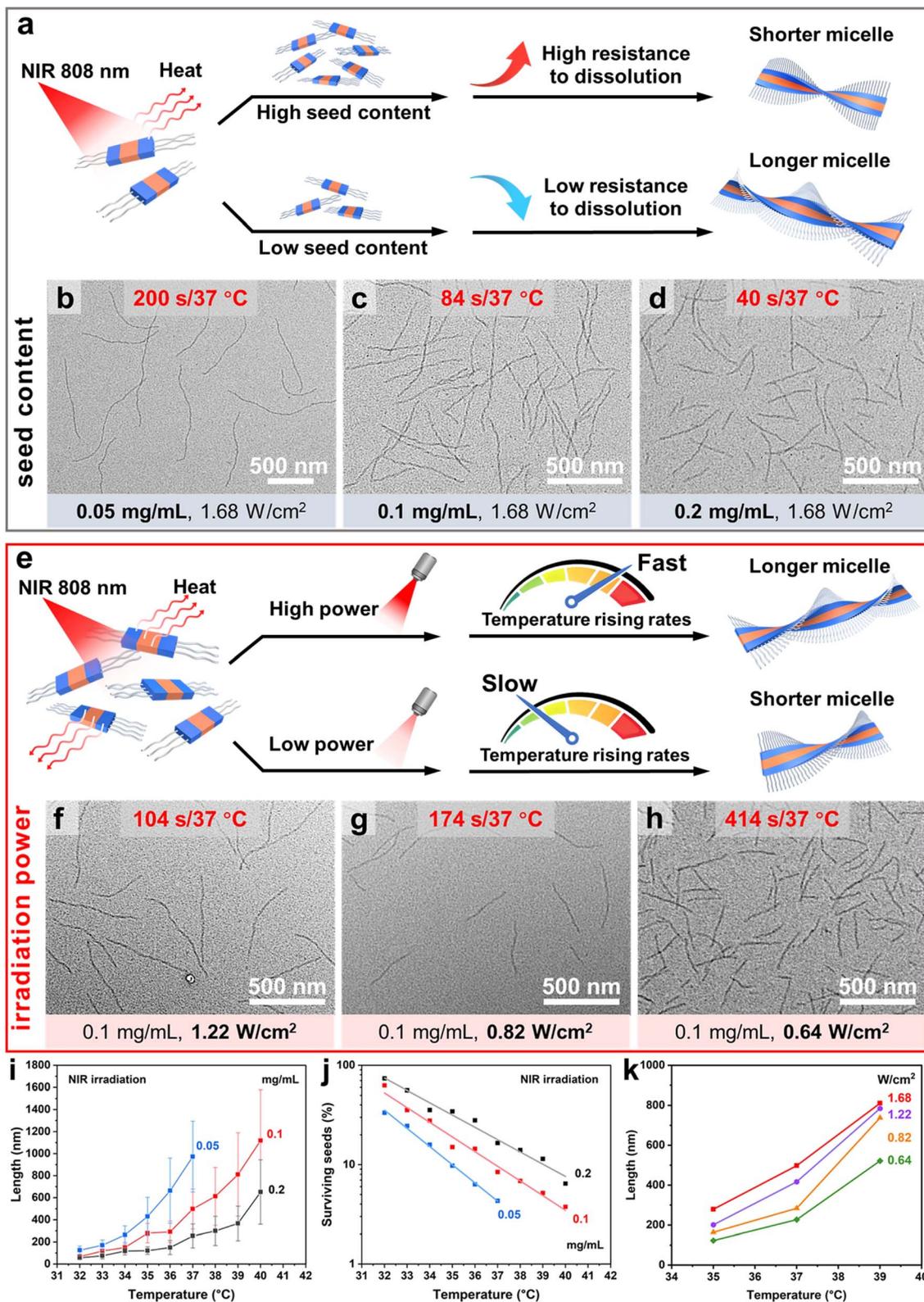
Fig. 5 Controlled preparation of 4-BBT-OPE₃-containing nanofibers by NIR regulated self-seeding. Schematic illustration of NIR regulated self-seeding of 4-BBT-OPE$_3$-b-P2VP$_{22}$ (a) with different seed concentrations and (e) under varying irradiation powers. TEM images of micelles of 4-BBT-OPE$_3$-b-P2VP$_{22}$ formed by NIR light at 37 °C with an irradiation power of 1.68 W cm^{-2} and the contents of (b) 0.05, (c) 0.1 and (d) 0.2 mg mL^{-1}. TEM images of micelles of 4-BBT-OPE$_3$-b-P2VP$_{22}$ (0.10 mg mL^{-1}) formed at 37 °C with an irradiation power of (f) 1.22, (g) 0.82 and (h) 0.64 W cm^{-2}. Dependence of (i) L_n of micelles of 4-BBT-OPE$_3$-b-P2VP$_{22}$ and (j) fraction of surviving seeds on annealing temperature obtained by NIR light regulated self-seeding with different contents of seed micelles (1.68 W cm^{-2}). (k) Dependence of L_n of micelles of 4-BBT-OPE$_3$-b-P2VP$_{22}$ formed by NIR light regulated self-seeding on the heating temperature with different irradiation power.

cooling/aging at 25 °C for 48 h. Uniform fiber-like micelles with L_w/L_n below 1.20 were obtained (Fig. 5b–d, S39, S40, Tables S3 and S4). The L_n of the resulting micelles also increased with the annealing temperature (irradiation time), and the fraction of seed micelles decreased exponentially with the increase of heating temperature (Fig. 5i, j, S41 and Tables S2–S4). We also tested the self-seeding of 4-BBT-OPE₃-*b*-P2VP₂₂ by direct heating at concentrations of 0.05 and 0.2 mg mL⁻¹ (Fig. S42–S44). Here, too, we observed a similar trend for the variation of L_n of the resulting micelles for direct heating and for NIR light regulated self-seeding (Fig. S42, S43 and Tables S5–S7). From these results, we note that, as the content of seed micelles increased, less irradiation time was required to reach the same temperature of the micellar solutions. We also note that, at the same annealing temperature, L_n values of micelles obtained with different seed contents decreased with the increase in seed concentration (Fig. 5a–d, i, S44 and Tables S2–S4). For example, L_n values of the micelles obtained at a heating temperature of 37 °C by NIR irradiation were 973, 498 and 254 nm, respectively, for micelle concentrations of 0.05, 0.1 and 0.2 mg mL⁻¹ (Fig. 5b–d and Tables S2–S4). This phenomenon is due to the increased resistance of seed micelles toward dissolution with the increase in seed concentration and is consistent with previous reports (Fig. 5a).[58,67,68]

To examine the influence of irradiation power on NIR light regulated self-seeding, aliquots of seed micelles (Fig. 4b, L_n = 42 nm, L_w/L_n = 1.11, 0.1 mg mL⁻¹) were exposed to NIR laser irradiation (808 nm) with powers of 1.68, 1.22, 0.82, and 0.64 W cm⁻² for different times to let the temperature of the solutions increase from 26 °C to 35 °C, 37 °C and 39 °C, respectively (Fig. 5e and S44), followed by cooling/aging at 25 °C for 48 h. Uniform fiber-like micelles with L_w/L_n values below 1.22 were obtained under these different conditions (Fig. 5f–h, S45 and Table S8). It is interesting to note that at a common annealing temperature, L_n of the micelles decreased with decreasing irradiation power (Fig. 5k, S45 and Table S8). For example, at an annealing temperature of 37 °C, L_n of micelles formed after exposure to laser powers of 1.68, 1.22, 0.82, and 0.64 W cm⁻² were 498, 417, 284 and 227 nm, respectively (Fig. 5c, f–h and Table S8). We imagine that this is an example of a pre-annealing effect. Winnik and co-workers reported that the pre-annealing of core-crystalline micelle seeds would promote the crystallinity of the seeds and increase their resistance toward dissolution. In this way, pre-annealing of seeds would result in the formation of a larger number of surviving seeds upon heating and thus shorter micelles upon cooling.[69]

In the current case, a longer irradiation time was required to reach the same annealing temperature for the sample with lower irradiation power. For example, for the samples with the target annealing temperature of 37 °C, the irradiation times were 414, 174, 104 and 84 s for the irradiation powers of 0.64, 0.82, 1.22 and 1.68 W cm⁻², respectively (Fig. 5c, f–h and Table S8). We infer that a longer irradiation time with a lower irradiation power, that is a slower heating rate (Fig. S46), would promote the crystallinity of the core of the seed micelles through annealing at temperatures below the apparent melting temperature of the crystalline seed core. The increase in

crystallinity would enhance the resistance of seed micelles toward dissolution upon heating. To test this idea, seed micellar solutions (0.1 mg mL⁻¹) were heated from 26 °C to 37 °C at different heating rates, followed by cooling and aging at 25 °C for 48 h. We found that uniform fiber-like micelles were formed with L_n values of 259, 183, 169 and 135 nm for the heating rates of 3.7 °C min⁻¹, 1.8 °C min⁻¹, 1.2 °C min⁻¹ and 0.9 °C min⁻¹, respectively (Fig. S47). All these results suggest that more seeds survived, and the L_n of micelles formed at the same target annealing temperature decreased with the decrease of irradiation power (Fig. 5e).

Self-seeding of NIR transparent micelles was observed in the presence of a photothermal dye. The photothermal activity of 4-BBT-OPE₃-*b*-P2VP₂₂ is a consequence of the BBT component, but NIR irradiation heats the entire solution rather than operating locally on the micelles. The implication of this result is that one could achieve a similar effect by adding an appropriate NIR photothermal dye to a NIR-transparent micelle solution (Fig. 6a). To test this idea, we prepared seed micelles in ethanol of OPV₅-*b*-P2VP₄₂ (Fig. 6b and S48, L_n = 44 nm, L_w/L_n = 1.10, 0.05 mg mL⁻¹) as described previously.[70] These micelles do not absorb light at 808 nm (Fig. 6c). To this solution, we added indocyanine green (ICG, 0.01 mg mL⁻¹), a typical photothermally active dye (Fig. 6b and c).[71] We exposed the solution to NIR laser irradiation (808 nm) with a power of 1.68 W cm⁻² for different times of 20 s, 28 s, 40 s, 58 s and 112 s to let the temperature of the solutions reach 35 °C, 40 °C, 45 °C, 50 °C and 55 °C, respectively (Fig. S49), followed by cooling/aging at 25 °C for 48 h. Self-seeding occurred, leading to uniform fiber-like micelles (Fig. 6a and d–j). As the irradiation times were increased from 20 s to 112 s, the L_n of the fiber-like micelles increased from 53 nm to 304 nm (Fig. 6e–i and S49). These observations show the versatility of the NIR regulated self-seeding strategy. This approach is applicable not only to crystalline-coil block copolymers of 4-BBT-OPE₃-*b*-P2VP₂₂ with intrinsic photothermal activity, but also to other more typical coil-crystalline block copolymers without photothermal activity, though the NIR-regulated self-seeding behavior was dependent on both the photothermal properties of the added NIR dye and the self-seeding properties of coil-crystalline copolymers. Here, the temperature can be modulated with the assistance of an added photothermal dye.

Tissue penetration

While 4-BBT-OPE₃-*b*-P2VP₂₂ is insoluble in water and has no obvious biomedical activity, it enables model experiments to show how NIR-responsive core-crystalline micelles might take advantage of the ability of NIR light to penetrate deep into biological tissue. As a proof-of-concept experiment, aliquots of seed micelles were placed under slices of chicken breast with different thicknesses of 1, 2, 3 and 4 mm (Fig. 7a, the experimental setup is shown in Fig. S50). These samples were then subjected to 808 nm laser irradiation for varying times to let the solution temperature reach 38 °C, followed by cooling and aging at 25 °C for 48 h. TEM analysis of the resulting samples showed that uniform fiber-like micelles had formed with L_n values of
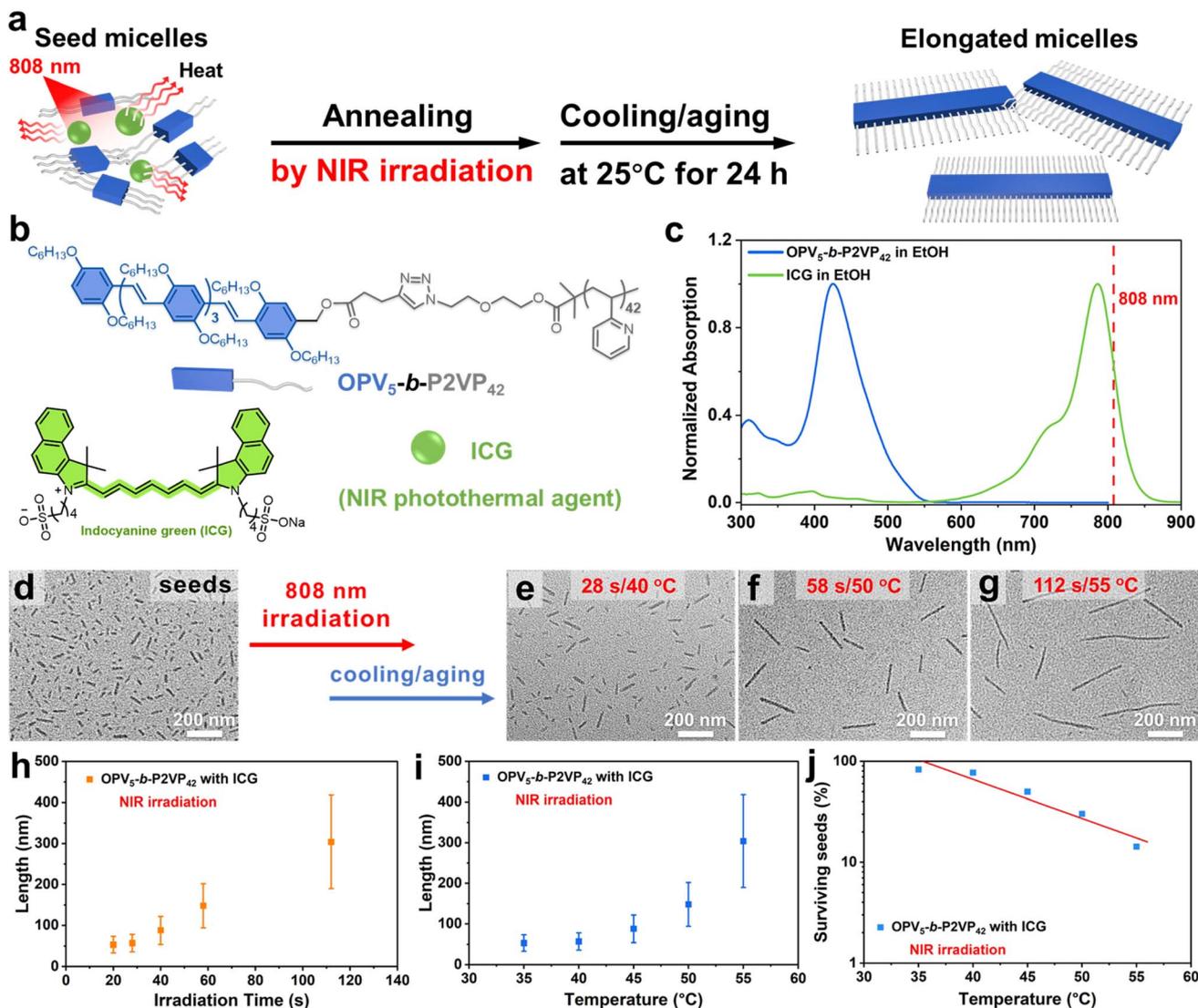
Fig. 6 NIR regulated self-seeding of OPV$_5$-containing BCPs in the presence of a photothermal dye. (a) Schematic illustration of NIR light regulated self-seeding of OPV$_5$-b-P2VP$_{42}$ in the presence of a NIR-active photothermal dye. (b) Structures of the coil-crystalline block copolymer OPV$_5$-b-P2VP$_{42}$ and the NIR photothermal agent ICG. (c) UV-vis-NIR absorption spectra of OPV$_5$-b-P2VP$_{42}$ and ICG in ethanol. TEM images of (d) seed micelles of OPV$_5$-b-P2VP$_{42}$ and micelles (0.05 mg mL^{-1}) obtained by of NIR light irradiation in the presence of ICG (0.01 mg mL^{-1}) for (e) 28 s, (f) 58 s and (g) 112 s. Dependence of L_n of micelles of OPV$_5$-b-P2VP$_{42}$ on (h) NIR irradiation time and (i) heating temperature. (j) Dependence of the fraction of surviving seed micelles on the heating temperature in NIR light regulated self-seeding of OPV$_5$-b-P2VP$_{42}$ in the presence of ICG.

434, 303, 251 and 220 nm for the samples irradiated, respectively, through 1, 2, 3 and 4 mm of chicken tissue (Fig. 7b, d–g and Table S9). For this range of tissue thicknesses and 1.68 W cm^{-2} as the NIR irradiation source, we found that the "working" irradiation powers were 0.96, 0.70, 0.41 and 0.32 W cm^{-2} (Fig. 7c). This attenuation of irradiation was mainly due to the light scattering effect induced by the chicken tissue[72] and resulted in longer times to reach the target temperature with the increase of tissue thickness (Fig. 7d–g).

As in the case of direct irradiation of micelle samples with decreasing laser irradiation power, we found that L_n of micelles formed at the same target temperature (38 °C) decreased with the increased thickness of chicken tissue (Fig. 7b). We infer that the longer irradiation (heating) time resulted in higher

crystallinity of the micelle seed cores, leading to less polymer dissolution upon heating and the formation of a larger number of shorter micelles upon cooling (Fig. 5k and Table S8).[69]

To further demonstrate the merit of spatial selectivity in a proof-of-concept manner, 20 μL aliquots of a micellar solution of 4-BBT-OPE$_3$-b-P2VP$_{22}$ (0.5 mg mL^{-1} in ethanol) were injected into slices of commercial chicken breast tissue (obtained from One's Member Supermarket) at a depth of around 2 mm, followed by exposure to NIR irradiation (808 nm and 1.68 W cm^{-2}). The local temperature of the injection spots increased to 33.9 °C, 38.1 °C, 40.8 °C and 44.6 °C after 10 s, 30 s, 60 s and 120 s of irradiation, respectively (Fig. 7h). All these results indicated that the NIR light regulated self-seeding strategy was endowed with excellent tissue penetration capacity and spatial selectivity.
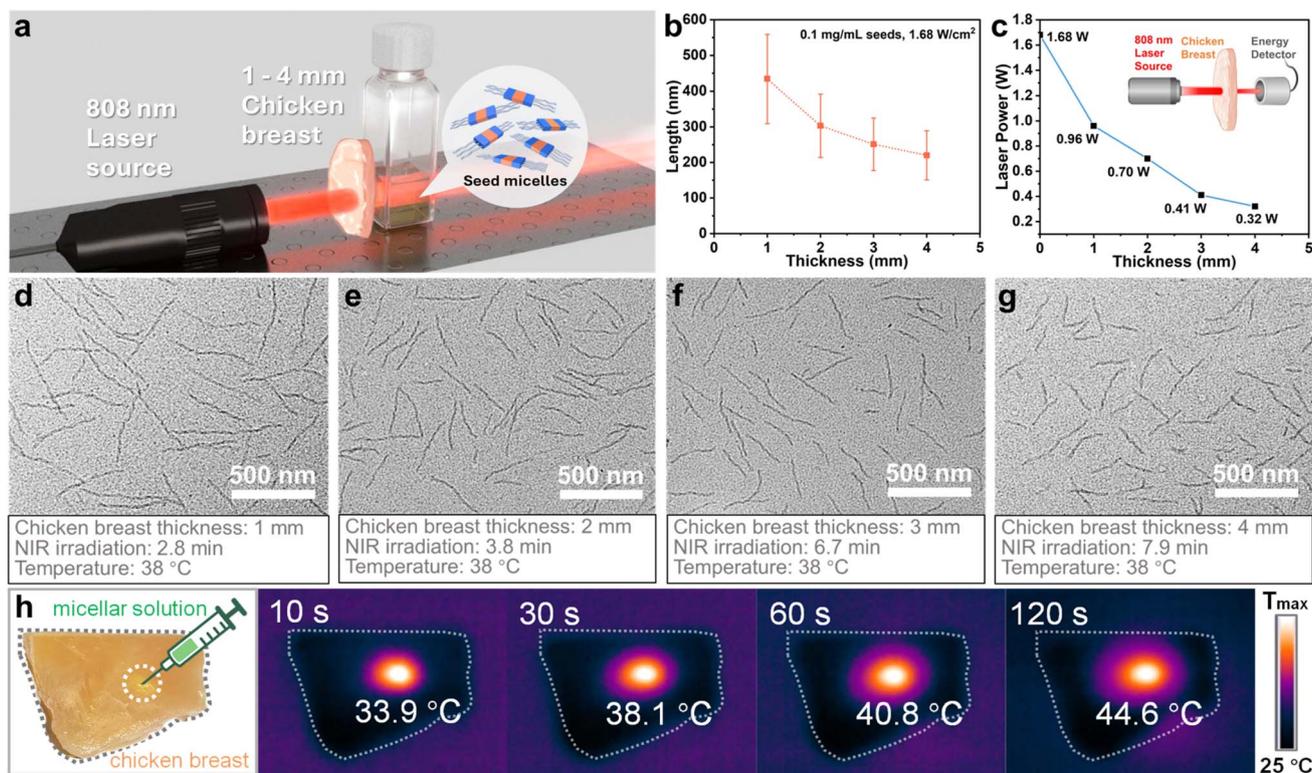
Fig. 7 Tissue penetration and spatial selectivity of 4-BBT-OPE$_3$-containing nanofibers. (a) Schematic illustration of the set-up for NIR light regulated self-seeding using slices of chicken breast as a model for tissue penetration. (b) Dependence of L_n of micelles on the thickness of chicken breast tissue. (c) Output intensity of the 808 nm laser passing through chicken tissue with different thicknesses (0–4 mm). TEM images of micelles obtained when the NIR light source was passed through slices of chicken tissue with thicknesses of (d) 1, (e) 2, (f) 3 and (g) 4 mm, respectively. (h) Photothermal images of chicken breast tissue injected with a micellar solution of 4-BBT-OPE$_3$-b-P2VP$_{22}$ (20 μL and 0.5 mg mL^{-1} in ethanol) during continuous 808 nm laser irradiation.

Conclusions

Polydisperse helical fiber-like micelles of 4-BBT-OPE$_3$-b-P2VP$_{22}$ were generated by a heating/cooling protocol in ethanol with equal amounts of left- and right-handed isomers and a regular pitch of ∼67 nm. The 4-BBT-OPE$_3$ units within the core adopted a two-column packing mode with a packing distance of 0.35 nm and a rotation angle of 0.9° to form the helical micelles. These micelles not only showed photothermal activity, but also upon irradiation with a 780 nm laser exhibited an NIR-II emission band that tailed to more than 1300 nm. The micelles showed no sign of photo-bleaching or photo-decomposition upon irradiation with 808 nm light. By leveraging the crystallinity and photothermal activity of the 4-BBT-OPE$_3$ segment, uniform fiber-like micelles with lengths up to 1.1 μm were generated, and the length of the micelles could be regulated by the time and power of the 808 nm NIR light. NIR light could also be used to induce self-seeding for solutions of micelles like OPV$_5$-b-P2VP$_{42}$ that are transparent at 808 nm if the irradiation was conducted in the presence of a NIR-active dye like indocyanine green.

NIR light can penetrate biological tissues. As a proof-of-concept experiment, we showed that the length of fiber-like micelles could be modulated even if the light source was blocked by slices of chicken breast with thicknesses up to 4 mm.

Given the versatility of living CDSA to manipulate the morphology and dimensions of self-assembled structures, the combination of NIR light and the intriguing properties of π-conjugated polymers holds promise for the creation of smart π-conjugated nanostructures with potential applications ranging from biomedicine to optoelectronics.

Author contributions

C. F., X. Y. H. and R. C. conceived the project and designed the experiments. R. C. carried out the synthesis, self-assembly, and other characterization experiments. R. C., S. Z. and G. L. L. analyzed the data and co-wrote the manuscript with input from C. F., X. Y. H. and M. A. W. C. F., and X. Y. H. supervised the project. All authors discussed the results and commented on the manuscript.

Conflicts of interest

The authors declare no competing interests.

Data availability

The data, including figures and tables, supporting this article have been included as part of the supplementary information

(SI). Further information and requests for resources and reagents should be directed to the Lead Contact, Chun Feng (cfeng@sioc.ac.cn) or Xiaoyu Huang (xyhuang@sioc.ac.cn). Supplementary information is available. See DOI: https://doi.org/10.1039/d6sc00684a.

Acknowledgements

References

1 D. Philp and J. F. Stoddart, *Angew. Chem., Int. Ed.*, 1996, **35**, 1154–1196.

2 J. Zhang, Y. Wang, B. J. Rodriguez, R. Yang, B. Yu, D. Mei, J. Li, K. Tao and E. Gazit, *Chem. Soc. Rev.*, 2022, **51**, 6936–6947.

3 W. Xia, Z. Xu, H. Dong, S. Zhang, C. He, D. Li, B. Sun, B. Dai, S. Dong and C. Liu, *J. Am. Chem. Soc.*, 2025, **147**, 20132–20143.

4 J. Rodríguez-Hernández, F. Chécot, Y. Gnanou and S. Lecommandoux, *Prog. Polym. Sci.*, 2005, **30**, 691–724.

5 S. Kang, G.-H. Kim and S.-J. Park, *Acc. Chem. Res.*, 2022, **55**, 2224–2234.

6 X. Liu, W. Zhan, G. Gao, Q. Jiang, X. Zhang, H. Zhang, X. Sun, W. Han, F.-G. Wu and G. Liang, *J. Am. Chem. Soc.*, 2023, **145**, 7918–7930.

7 L. R. MacFarlane, H. Shaikh, J. D. Garcia-Hernandez, M. Vespa, T. Fukui and I. Manners, *Nat. Rev. Mater.*, 2021, **6**, 7–26.

8 S. T. G. Street, Y. He, X.-H. Jin, L. Hodgson, P. Verkade and I. Manners, *Chem. Sci.*, 2020, **11**, 8394–8408.

9 L. MacFarlane, C. Zhao, J. Cai, H. Qiu and I. Manners, *Chem. Sci.*, 2021, **12**, 4661–4682.

10 M. Elsabahy and K. L. Wooley, *Chem. Soc. Rev.*, 2012, **41**, 2545–2561.

11 Y. Zhang, J. Tian, H. Shaikh, H. K. MacKenzie, Y. He, C. Zhao, S. Lei, Y. Ren and I. Manners, *J. Am. Chem. Soc.*, 2023, **145**, 22539–22547.

12 Y. Geng, P. Dalhaimer, S. Cai, R. Tsai, M. Tewari, T. Minko and D. E. Discher, *Nat. Nanotechnol.*, 2007, **2**, 249–255.

13 H. C. Parkin, S. T. G. Street, B. Gowen, L. H. Da-Silva-Correa, R. Hof, H. L. Buckley and I. Manners, *J. Am. Chem. Soc.*, 2024, **146**, 5128–5141.

14 M. A. Beach, U. Nayanathara, Y. Gao, C. Zhang, Y. Xiong, Y. Wang and G. K. Such, *Chem. Rev.*, 2024, **124**, 5505–5616.

15 D. Wei, Y. Sun, H. Zhu and Q. Fu, *ACS Nano*, 2023, **17**, 23223–23261.

16 F. Xu and B. L. Feringa, *Adv. Mater.*, 2023, **35**, 2204413.

17 S. Song, H. Zhang and Y. Liu, *Acc. Chem. Res.*, 2024, **5**, 1109–1120.

18 Y. Wang, Y. Yuan, S. Zhang, L. Chen and Y. Chen, *Chin. J. Chem.*, 2024, **42**, 3278–3282.

19 R. Klajn, *Chem. Soc. Rev.*, 2014, **43**, 148–184.

20 V. J. Pereira, H. S. Weinberg, K. G. Linden and P. C. Singer, *Environ. Sci. Technol.*, 2007, **41**, 1682–1688.

21 S. Nešpůrek and J. Pospíšil, *J. Optoelectron. Adv. Mater.*, 2005, **7**, 1157–1168.

22 S. Pearson, J. Feng and A. del Campo, *Adv. Funct. Mater.*, 2021, **31**, 2105989.

23 Z. Liu, Y. Yao, X. Tao, J. Wei and S. Lin, *ACS Macro Lett.*, 2021, **10**, 1174–1179.

24 S. Chen, R. Costil, F. K.-C. Leung and B. L. Feringa, *Angew. Chem., Int. Ed.*, 2021, **60**, 11604–11627.

25 Y. Ren, J. Gao, T. Cai, L. Liu, H. Huang, Y. Guo, X. Hou, Y. Lu and L. Jia, *Angew. Chem., Int. Ed.*, 2025, **64**, e202511365.

26 S. Shin, F. Menk, Y. Kim, J. Lim, K. Char, R. Zentel and T.-L. Choi, *J. Am. Chem. Soc.*, 2018, **140**, 6088–6094.

27 J. Zhang, T. Xiao, Z. Liu, Y. Yin, C. Li, F. Xu and Y. Mai, *J. Am. Chem. Soc.*, 2025, **147**, 19148–19156.

28 S. K. Patra, R. Ahmed, G. R. Whittell, D. J. Lunn, E. L. Dunphy, M. A. Winnik and I. Manners, *J. Am. Chem. Soc.*, 2011, **133**, 8842–8845.

29 J. Jiang and M. A. Winnik, *Acc. Chem. Res.*, 2025, **58**, 1683–1695.

30 H. Kim, J. Lee, S.-H. Hwang, N. Yun, S. Park and T.-L. Choi, *J. Am. Chem. Soc.*, 2024, **146**, 20750–20757.

31 J. Qian, G. Guerin, Y. Lu, G. Cambridge, I. Manners and M. A. Winnik, *Angew. Chem., Int. Ed.*, 2011, **50**, 1622–1625.

32 J. Ma, G. Lu, X. Huang and C. Feng, *Chem. Commun.*, 2021, **57**, 13259–13274.

33 L. Han, M. Wang, X. Jia, W. Chen, H. Qian and F. He, *Nat. Commun.*, 2018, **9**, 865.

34 L. Han, H. Fan, Y. Zhu, M. Wang, F. Pan, D. Yu, Y. Zhao and F. He, *CCS Chem.*, 2020, **3**, 1399–1409.

35 K. Narasimha, S. K. Albert, J. Kim, H. Kang, S. Kang, J. Park, J. Park and S.-J. Park, *ACS Macro Lett.*, 2023, **12**, 382–388.

36 M. C. Arno, M. Inam, Z. Coe, G. Cambridge, L. J. Macdougall, R. Keogh, A. P. Dove and R. K. O'Reilly, *J. Am. Chem. Soc.*, 2017, **139**, 16980–16985.

37 T. Xia, Z. Tong, Y. Xie, M. C. Arno, S. Lei, L. Xiao, J. Y. Rho, C. T. J. Ferguson, I. Manners, A. P. Dove and R. K. O'Reilly, *J. Am. Chem. Soc.*, 2023, **145**, 25274–25282.

38 Z. Tong, Y. Xie, M. C. Arno, Y. Zhang, I. Manners, R. K. O'Reilly and A. P. Dove, *Nat. Chem.*, 2023, **15**, 824–831.

39 S.-H. Hwang, S.-Y. Kang, S. Yang, J. Lee and T.-L. Choi, *J. Am. Chem. Soc.*, 2022, **144**, 5921–5929.

40 C. Wang, L. Xu, L. Zhou, N. Liu and Z.-Q. Wu, *Angew. Chem., Int. Ed.*, 2022, **61**, e202207028.

41 L. Xu, C. Wang, Y.-X. Li, X.-H. Xu, L. Zhou, N. Liu and Z.-Q. Wu, *Angew. Chem., Int. Ed.*, 2020, **59**, 16675–16682.

42 S. Song, H. Zhou, S. Ye, J. Tam, J. Y. Howe, I. Manners and M. A. Winnik, *Angew. Chem., Int. Ed.*, 2021, **60**, 10950–10956.

43 S. Yang and T.-L. Choi, *Chem. Sci.*, 2020, **11**, 8416–8424.

44 L. Sun, Y. Wang, F. Yang, X. Zhang and W. Hu, *Adv. Mater.*, 2019, **31**, 1902328.

45 B. Jin, K. Sano, S. Aya, Y. Ishida, N. Gianneschi, Y. Luo and X. Li, *Nat. Commun.*, 2019, **10**, 2397.

46 B. Jin, Q. Li, L. Hu, Q. Liu, Y. Chen, Y. Luo, S. Chi and X. Li, *Angew. Chem., Int. Ed.*, 2023, **62**, e202219067.

47 H. Qiu, Y. Gao, V. A. Du, R. Harniman, M. A. Winnik and I. Manners, *J. Am. Chem. Soc.*, 2015, **137**, 2375–2385.

48 C. Duan, B. Xu, R. Li, X. Huang, S. Lin and C. Feng, *Sci. China Chem.*, 2024, **67**, 2341–2352.

49 D. Li, X. Chen, D. Wang, H. Wu, H. Wen, L. Wang, Q. Jin, D. Wang, J. Ji and B. Z. Tang, *Biomaterials*, 2022, **283**, 121476.

50 D. Xi, M. Xiao, J. Cao, L. Zhao, N. Xu, S. Long, J. Fan, K. Shao, W. Sun, X. Yan and X. Peng, *Adv. Mater.*, 2020, **32**, 1907855.

51 T. Liu, C. Wang, J. Ma, C. Yan, W. Zhang, M. Li, G. Zhang, H. Huang and W. Huang, *Chin. J. Chem.*, 2025, **43**, 2298–2306.

52 J. Ma, B. Hao, S. Zhang, X. Huang, G. Lu and C. Feng, *Adv. Mater. Interfaces*, 2022, **9**, 2201823.

53 J. Ma, F. Huang, S. Zhang, J. Ye, X. Huang, G. Lu and C. Feng, *Macromolecules*, 2023, **56**, 8529–8546.

54 F. Huang, J. Ma, J. Nie, B. Xu, X. Huang, G. Lu, M. A. Winnik and C. Feng, *J. Am. Chem. Soc.*, 2024, **146**, 25137–25150.

55 H. Wang, W. You, P. Jiang, L. Yu and H. H. Wang, *Chem.–Eur. J.*, 2004, **10**, 986–993.

56 H. Sun, *J. Phys. Chem. B*, 1998, **102**, 7338–7364.

57 H. Sun, P. Ren and J. R. Fried, *Comput. Theor. Polym. Sci.*, 1998, **8**, 229–246.

58 D. Tao, C. Feng, Y. Lu, Y. Cui, X. Yang, I. Manners, M. A. Winnik and X. Huang, *Macromolecules*, 2018, **51**, 2065–2075.

59 M. J. Gonzalez-Alvarez, L. Jia, G. Guerin, K. S. Kim, V. An Du, G. Walker, I. Manners and M. A. Winnik, *Macromolecules*, 2016, **49**, 7975–7984.

60 W. Ji, B. Xue, S. Bera, S. Guerin, Y. Liu, H. Yuan, Q. Li, C. Yuan, L. J. W. Shimon, Q. Ma, E. Kiely, S. A. M. Tofail, M. Si, X. Yan, Y. Cao, W. Wang, R. Yang, D. Thompson, J. Li and E. Gazit, *ACS Nano*, 2020, **14**, 10704–10715.

61 F. Wang, R. Liao and F. Wang, *Angew. Chem., Int. Ed.*, 2023, **62**, e202305827.

62 L. Xiao, T. Xia, J. Zhang, S. J. Parkinson, J. Y. Rho, A. P. Dove and R. K. O' Reilly, *Nat. Synth.*, 2025, **4**, 808–815.

63 J. B. Gilroy, T. Gädt, G. R. Whittell, L. Chabanne, J. M. Mitchels, R. M. Richardson, M. A. Winnik and I. Manners, *Nat. Chem.*, 2010, **2**, 566–570.

64 J. Qian, Y. Lu, G. Cambridge, G. Guerin, I. Manners and M. A. Winnik, *Macromolecules*, 2012, **45**, 8363–8372.

65 C. Ma, D. Tao, Y. Cui, X. Huang, G. Lu and C. Feng, *Macromolecules*, 2020, **53**, 8631–8641.

66 G. Guérin, H. Wang, I. Manners and M. A. Winnik, *J. Am. Chem. Soc.*, 2008, **130**, 14763–14771.

67 Y. Cui, Z. Wang, X. Huang, G. Lu, I. Manners, M. A. Winnik and C. Feng, *Macromolecules*, 2020, **53**, 1831–1841.

68 G. Guerin, G. Molev, D. Pichugin, P. A. Rupar, F. Qi, M. Cruz, I. Manners and M. A. Winnik, *Macromolecules*, 2019, **52**, 208–216.

69 J. Qian, Y. Lu, A. Chia, M. Zhang, P. A. Rupar, N. Gunari, G. C. Walker, G. Cambridge, F. He, G. Guerin, I. Manners and M. A. Winnik, *ACS Nano*, 2013, **7**, 3754–3766.

70 Z. Wang, C. Ma, X. Huang, G. Lu, M. A. Winnik and C. Feng, *Macromolecules*, 2021, **54**, 6705–6717.

71 N. Kwon, G. O. Jasinevicius, G. Kassab, L. Ding, J. Bu, L. P. Martinelli, V. G. Ferreira, A. Dhaliwal, H. H. L. Chan, Y. Mo, V. S. Bagnato, C. Kurachi, J. Chen, G. Zheng and H. H. Buzzá, *Angew. Chem., Int. Ed.*, 2023, **62**, e202305564.

72 J. Zhang, H. Xia, X. Zhou, Z. Meng, Q. Jin, D. Chen, X. Xia, Y. Jiao, J. Chang, Z. Dong, Z. Zeng, H. Ma and C. Yang, *Mater. Today Bio*, 2025, **31**, 101577.